Article

Spatial transcriptomic analysis drives PET imaging of tight junction protein expression in pancreatic cancer theranostics

James Wang[1,9], Jai Woong Seo [1,9], Aris J. Kare [1,2,9], Martin Schneider [1], Mallesh Pandrala[1], Spencer K. Tumbale [1], Marina N. Raie [1], Gokce Engudar[1], Nisi Zhang [1], Yutong Guo[1], Xiaoxu Zhong [3], Sofia Ferreira [3], Bo Wu[1], Laura D. Attardi [3,4], Guillem Pratx [3], Andrei Iagaru[5], Ryan L. Brunsing[6], Gregory W. Charville [7], Walter G. Park[8] & Katherine W. Ferrara [1] ✉

Molecular imaging using positron emission tomography (PET) provides sensitive detection and mapping of molecular targets. While cancer-associated fibroblasts and integrins have been proposed as targets for imaging of pancreatic ductal adenocarcinoma (PDAC), herein, spatial transcriptomics and proteomics of human surgical samples are applied to select PDAC targets. We find that selected cancer cell surface markers are spatially correlated and provide specific cancer localization, whereas the spatial correlation between cancer markers and immune-related or fibroblast markers is low. Claudin-4 expression increases ~16 fold in cancer as compared with normal pancreas, and tight junction localization confers low background for imaging in normal tissue. We develop a peptide-based molecular imaging agent targeted to claudin-4 with accumulation to ~25% injected activity per cubic centimeter (IA/cc) in metastases and ~18% IA/cc in tumors. Our work motivates a data-driven approach to selection of molecular targets.

Molecular Imaging (MI) is a growing biomedical discipline that enables the non-invasive visualization, characterization, and quantification of chemical and biological processes at the cellular and subcellular levels across time in living systems. Molecular imaging can detect small cancerous lesions and provides an opportunity to assess therapeutic accumulation across a wide range of molecular therapies. Positron emission tomography (PET) uniquely quantifies molecular targets by employing sub-pharmacological amounts of molecularly-specific radiolabeled agents (radiopharmaceuticals). The short radioactive half-lives used in PET imaging facilitate repeated imaging, and the latest hardware innovations enable dynamic, functional imaging of these biomarkers in situ.

Improved imaging methods are needed to map pancreatic ductal adenocarcinoma (PDAC) lesions and guide therapy. Characterizing pancreatic nodules with imaging is significant as 30-50% of the adult population may harbor precancerous lesions[1–4]. Invasive cancer can be present within intraductal papillary mucinous neoplasms (IPMNs), and similar mutational profiles to PDAC are found in incidentally-discovered pancreatic intraepithelial neoplasms (PanINs)[2]. Further, PDAC is the third leading cause of cancer-related deaths as of 2024[5].

[1]Molecular Imaging Program at Stanford, Department of Radiology, Stanford University, 300 Pasteur Drive, Stanford, CA, USA. [2]Department of Bioengineering, Stanford University, 443 Via Ortega, Stanford, CA, USA. [3]Department of Radiation Oncology, Stanford University, 857 Blake Wilbur Drive, Stanford, CA, USA. [4]Department of Genetics, Stanford University, 291 Campus Drive, Stanford, CA, USA. [5]Nuclear Medicine and Molecular Imaging Division, Department of Radiology, Stanford University, 300 Pasteur Drive, Stanford, CA, USA. [6]Department of Radiology, Stanford University, 300 Pasteur Drive, Stanford, CA, USA. [7]Department of Pathology, Stanford University, 300 Pasteur Drive, Stanford, CA, USA. [8]Department of Medicine-Gastroenterology & Hepatology, Stanford University, 300 Pasteur Drive, Stanford, CA, USA. [9]These authors contributed equally: James Wang, Jai Woong Seo, Aris J. Kare. ✉e-mail: kwferrar@stanford.edu

PET-CT imaging has been applied using ^{18}F-FDG imaging of metabolism[6–8]; however, ^{18}F-FDG has low sensitivity and specificity in the diagnosis of PDAC with variable detection of metastatic lymph nodes and false-positive findings in inflammation[9,10].

Cell surface receptors are preferred for imaging and therapy due to the relative efficiency of delivery, where an ideal agent will safely accumulate within minutes while excess agent is rapidly cleared from the body, facilitating imaging and minimally-toxic therapies. PDAC markers currently under study for PET imaging, including integrins and fibroblast markers, are expressed by only a fraction of tumor cells (e.g. ITGB6, in 49% of PDAC cells[11]) and have substantial background in many cases[11].

Claudin-4 (CLDN4) is a cell surface protein that is buried within cell-cell junctions in healthy tissue and has been suggested as a cancer biomarker[12]. CLDN4 expression increases in PDAC, and enhanced CLDN4 expression disrupts other claudin family molecules in forming polymeric strands constituting the tight junction[13]. Increased CLDN4 expression thus results in the loss of tight junction integrity[14], and we hypothesized that the junction protein would be exposed to a radio-oligand in the presence of disease due to the loss of junctional integrity in metastatic cells[12,15,16]. Previous literature indicates that 1) CLDN4 expression is also enhanced in prostate[17], breast[18] and ovarian[19] cancers and 2) as pancreatic precancers advance, the expression level of CLDN4 increases ($p = 0.001$)[15]. Intense positive CLDN4 immunolabeling has been noted within virtually all primary (71/72 [99%]) and metastatic (49/49 [100%]) PDAC tissue samples and in 10 of 11 precancerous PanIN specimens[20]. Additionally, CLDN4 is a surface protein that has been applied preclinically for optical tumor imaging[21]. Although Claudin-6 and -18.2 have been the basis for development of therapeutics for ovarian and esophageal/gastric cancers[22], Claudin 6 expression is not enhanced in PDAC, and Claudin-18.2 expression is lower in PDAC than that of CLDN4[11,20].

In our work, a multi-omics data-driven approach is shown to distill target receptors suitable for imaging in pancreatic cancer, improving upon past methods that lacked a data-driven basis for the comparative evaluation of target receptors. To compare and contrast the abundance and spatial distribution of potential molecular imaging targets, we first apply spatial transcriptomic methods in human surgical specimens to assess mRNA expression across cell surface markers upregulated in PDAC. While single-cell sequencing data sets can validate abundance, spatial transcriptomics provides the opportunity to determine whether the target is consistently upregulated in cells with a cancerous phenotype across the tumor. We further evaluate the pseudotime evolution of the precancers and cancer to prioritize markers that are enhanced in invasive rather than precancerous lesions. Next, immune and fibroblast populations are profiled using spatial proteomics (codetection by indexing, CODEX) and immunohistochemistry (IHC) due to the need for single-cell resolution when exploring such targets. These analyses confirm that the epithelial tumor marker abundance and consistency are higher than immune and fibroblast markers across patients. As a result of the spatial multi-omic analyses, Claudin-4 (CLDN4) is identified as a particularly attractive imaging target. Based on our analyses of human tissue, we design a peptide target radiopharmaceutical and image CLDN4 expression in multiple models of murine PDAC.

Results

Spatial sequencing of PDAC samples elucidates spatially-correlated cancer surfaceome markers

Our discovery cohort includes 40 human surgical samples of surrounding pancreas, IPMNs[23] or PDAC[24] acquired at Stanford ($n = 12$ Visium and associated CODEX and IHC data for these samples) or from publicly-available databases ($n = 28$ Visium)[23,24] (Supplementary Table 1, Fig. 1A) and annotated single-cell RNA sequencing results from reference databases[24–26]. All human data collection and analysis was approved by the Stanford Institutional Review Board. The spatial transcriptomics samples span precancers, naïve untreated PDAC, and patients treated with chemotherapy or chemo-radiation or mixed treatment. We first integrated data from treatment-naïve PDAC samples and performed unsupervised clustering (Supplementary Fig. 1, Fig. 1A, B). We leveraged Seurat's integration method, which uses canonical correlation analysis and alignment based on mutual nearest neighbors to address batch differences[27]. Top genes in all spatial clusters are summarized in Supplementary Fig. 1B, C, whereas Fig. 1B–H focuses on the top surfaceome atlas markers in the cancer cluster. Since we seek to develop an imaging ligand that binds to PDAC cells, we filtered the cancer surfaceome to identify genes with enhanced expression in more than 80% of PDAC cells (Supplementary Table 2) as our cancer surfaceome gene list. Given that Visium transcriptomic spots contain multiple cells, we then performed hypergeometric t tests (Supplementary Fig. 1D) to determine the significance and overlap of differentially expressed genes and single-cell RNA cell signatures[24,25]. Cluster 1 is primarily enriched in tumor cell signature genes, with secondary enrichment in fibroblasts and ductal cells, underscoring the tumor environment consisting of ductal cells and fibroblasts (Fig. 1C)[28]. In particular, Cluster 1 differentially expressed S100P, MUC5AC, TFF1 and CLDN4 as compared with other clusters and surrounding normal pancreas (Fig. 1D).

Since cancer development is associated with increased copy number variation (CNV), we computed CNV from our transcriptomic data across the clusters and found that Cluster 1 had greater CNV gains compared to other clusters (Supplementary Fig. 2A). Single-cell RNA tumor signatures based on[24,25] and applied across clusters also confirmed that tumor signature genes are upregulated in Cluster 1 from PDAC samples (Supplementary Fig. 2B).

To quantify how top cancer surfaceome atlas markers change across clusters (Supplementary Table 3), we created a cancer surfaceome score based on the summed average of normalized and scaled expression of cancer cell surfaceome genes in each cluster. The cancer cell surfaceome expression levels differed among clusters and were upregulated in Cluster 1 (Fig. 1E). The correlation of a set of the cancer surfaceome epithelial markers with one another (CLDN4, GRPC5A, S100P, TSPAN8, MUC1, TFF1) was > 0.6 averaged across all spatial locations in the naïve PDAC cohort (Fig. 1F). CLDN4 is involved in tight junction formation, which is compromised during cancer progression. Positive correlation among cancer surface protein encoding genes indicates that CLDN4 expression changes are spatially correlated with other cancer-associated genes. Merging scaled and normalized data across transcriptomic sets from Stanford and HTAN, the fraction of spots in Cluster 1 overexpressing CLDN4, S100P, TFF1, CEACAM5, MUC5AC and fibroblast activation protein (FAP) was 89, 78, 57, 46, 60 and 27%, respectively. With integration of batch-corrected data from Stanford and HTAN[24] (rather than merging the datasets across sites), the fraction of spots with CLDN4 overexpression increased to 97.5%, and differences across key genes were consistent. We performed differential analysis comparing Cluster 1 with the remaining clusters and explored cancer surfaceome genes with an average $\log_2$ fold change greater than 2 and a p value less than 0.005. Based on the integrated gene expression, CLDN4 was upregulated to a greater extent than other genes in Cluster 1 with an average $\log_2$ fold change of 13.9 and a p value less than 7.6×10^{-300} (Supplementary Table 3).

S100P, a largely cytoplasmic protein, was used for comparison of the spatial distribution and expression of surfaceome markers as S100P expression is absent in normal pancreas, and a specific increase in S100P expression occurs only in the PDAC tumor epithelium[29]. S100P expression level in PDAC and IPMN is significantly higher than in nontumor pancreatic tissues, and its expression level increases with the grade of PanIN[30]. The Pearson's coefficient between cancer surfaceome genes and S100P was consistent within all spatial regions, with CLDN4 demonstrating the highest average coefficient (Fig. 1G). The Pearson's coefficient between S100P and various integrin markers or FAP ranged between −0.3 and 0.4 (highest scoring integrins are shown in Fig. 1G) and was 0.37 and 0.01 for ITGB6 and FAP, respectively.
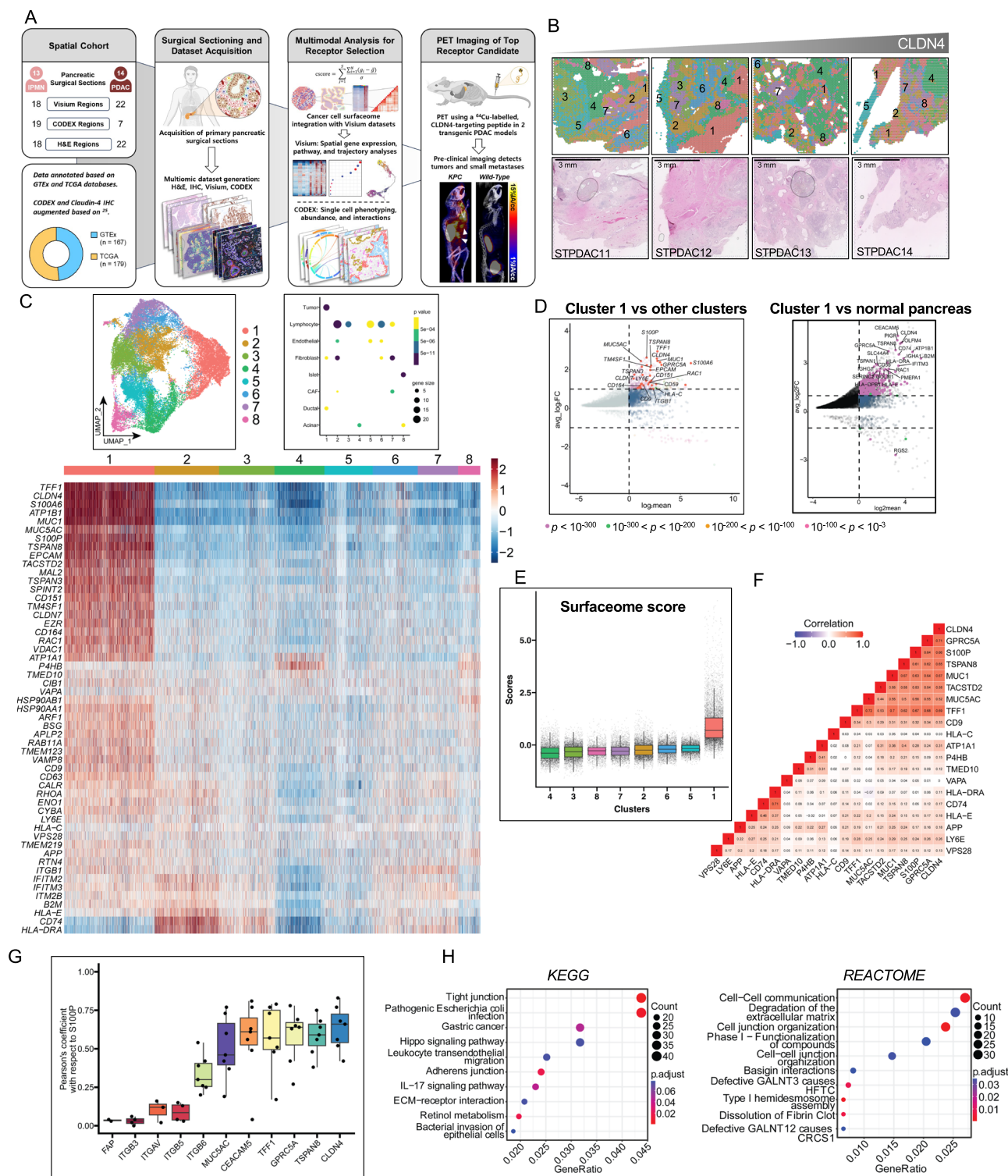
We then performed enrichment analysis (Fig. 1H) for these genes with respect to KEGG and REACTOME databases and found that Cluster 1 was enriched in tight junction (KEGG), IL-17 signaling (KEGG), and degradation of extracellular matrix (REACTOME) pathways, which implies significant stromal restructuring associated with Cluster 1.

High-resolution IHC indicated that CLDN4 protein expression was enhanced on hyperproliferative cells with a morphology consistent with cancer (Fig. 2A) (small to medium-sized irregular glands with nuclear atypia lacking tight junctions and embedded in a desmoplastic stroma). Proliferation (increased Ki67 expression) was enhanced in high-grade PanINs and cancerous ducts (Fig. 2B).

Alignment of hematoxylin and eosin (H&E) images with the mRNA expression of four key surface markers (Fig. 2C) confirms enhanced *CLDN4* expression in high-grade PanINs. While mRNA expression across *S100P*, *CLDN4*, *TFF1* and *CEACAM5* was highly correlated, expression on low-grade PanINs varied with phenotype (Fig. 2C). As shown in Fig. 2A and D, in addition to the upregulation of *CLDN4* in the cancer-associated cluster, molecular imaging of CLDN4 is attractive as the protein is more accessible on diseased cells (Fig. 2D). Taken together, the results suggest that *CLDN4* is consistently elevated in PDAC and is highly spatially correlated with cancer-associated markers. Alternatively, fibroblast, integrin and

Fig. 1 | Spatial transcriptomic characterization of human PDAC tissue slices.
A Overview of the project. Parts created with BioRender.com. **B** H&E of PDAC tumor excised from four patients (bottom row) and their corresponding spatial transcriptomic spots (top row) arranged based on increasing *CLDN4* expression. The spatial transcriptomes between the PDAC slices were integrated based on canonical correlation analysis (Seurat), clustered, projected on the Uniform Manifold Approximation and Projection (UMAP) dimension in (**C**), and projected onto their histology slices. Scale bar = 3 mm. **C** Leiden clustering of PDAC transcriptome projected on UMAP space and heatmap of Leiden clusters with genes selected from the PDAC data set of the cancer cell surfaceome with a specification of expression on at least 80% of cells. Scale represents z-score of log-normalized gene counts. Cluster identities were determined with one-sided hypergeometric t tests of all clusters in PDAC with respect to cell type signatures detailed in refs. 24,25, which were derived from scRNA and plotted as a dotplot. **D** Differential expression of Cluster 1 versus all remaining

clusters and versus samples of unaffected pancreas surrounding precancerous IPMN. **E** Cancer surfaceome score based on average normalized and scaled gene expression of all cells and all cancer cell surfaceome pancreatic cancer genes in each cluster. **F** Pearson's correlation similarity matrix of select cancer cell surfaceome genes based on the PDAC spatial transcriptome. **G** Pearson's correlation of all spots for *S100P* vs key markers of interest. **H** KEGG and REACTOME pathway enrichment of Cluster 1. Each calculation was based on $n = 7$ samples. For box plots, the center is the median and the lower and upper bound of the box are 25% and 75% of the distribution, respectively. The lower whisker is the lower 25% −1.5 x interquartile range (IQR). The upper whisker is the upper 75% + 1.5 x IQR. Differential expression analysis in (**D**) and (**E**) were based on non-parametric Wilcoxon rank sum test, which is a default setting in Seurat's FindMarkers function. Gene enrichment analysis in (**H**) was done with 1-sided hypergeometric t test based on clusterProfiler package. Source data are provided as a Source Data file.
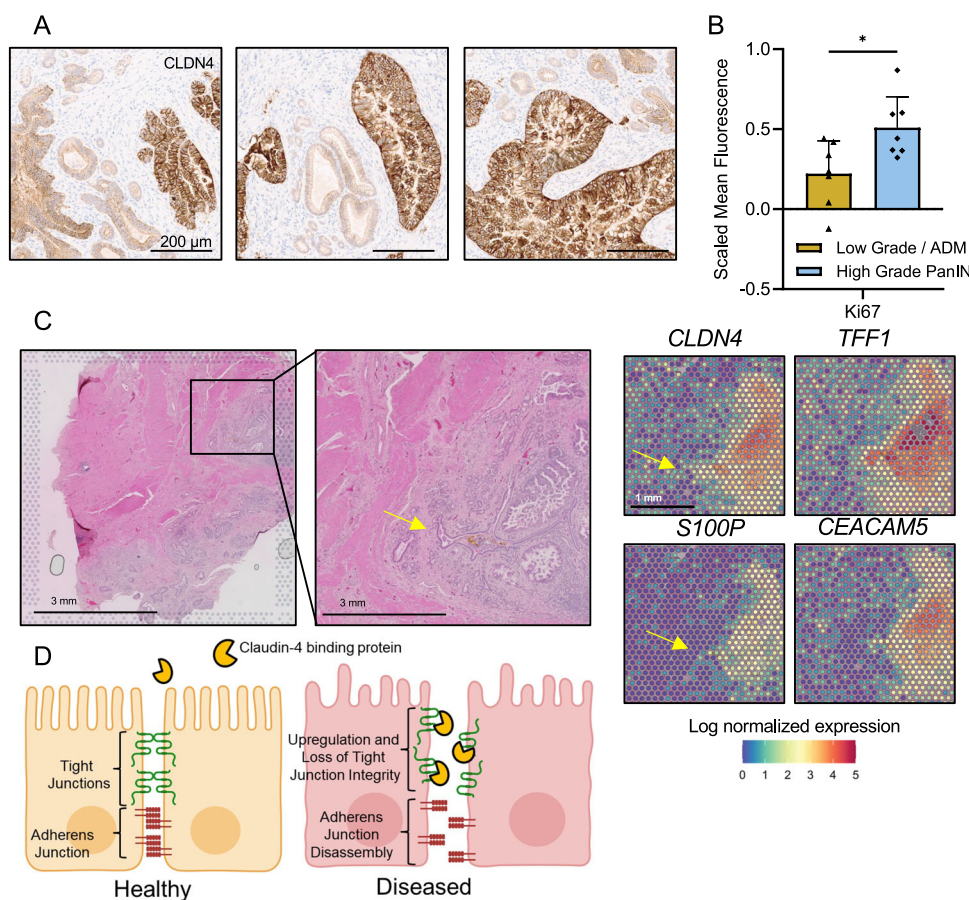

Fig. 2 | High-resolution protein imaging confirms selective expression of CLDN4 on high-grade PanINs and cancerous ducts. A High resolution CLDN4 immunohistochemistry (IHC) sections. **B** Ki67 quantification on high-grade pancreatic intraepithelial neoplasia (PanIN) vs low-grade PanIN/acinar-to-ductal metaplasia (ADM), **C** High-resolution hematoxylin and eosin (H&E) imaging compared with mRNA expression of *CLDN4*, *TFF1*, *S100P* and *CEACAM5* in the same region validates similar expression. Yellow arrows indicate small differences in low-grade lesions. **D** Illustrated summary of the changes in CLDN4 expression with

disease and the expected impact on the ability of peptides to target the protein. In healthy tissue, CLDN4 and adherens junction proteins form a tight cell-cell junction and are not accessible to imaging ligands. In diseased tissue the cell-cell junctions are compromised, displaying CLDN4 proteins to targeted imaging ligands. Created with BioRender.com. Significance analyzed with a two-sided unpaired t-test, * = $p < 0.05$ ($p = 0.0196$) in (**B**) and the whiskers represent standard deviation. **A**, **B**, **C** were based on a sample replicate of $n = 7$.
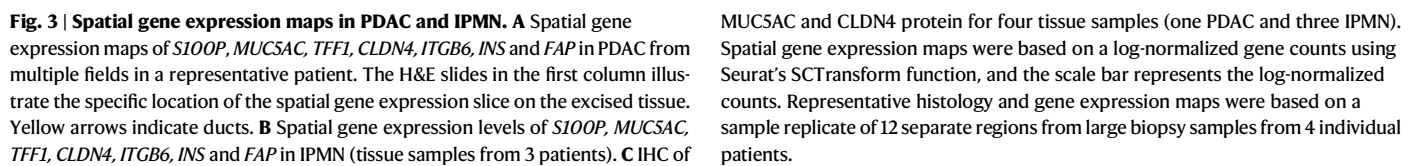
immune receptor markers were not spatially correlated with *S100P* or cancer atlas markers.

Key tumor epithelial marker expression is spatially correlated
We next visualized the spatial correlation between the top epithelial markers in PDAC and IPMNs and compared these maps with those relevant for islets and fibroblasts, where rows represent individual fields from a single patient sample (Fig. 3A). On the 100-μm spatial scale of spatial transcriptomic slides, we found that *S100P, MUC5AC, TFF1*

and *CLDN4* were spatially correlated and moreover, in regions where ducts were filled with large numbers of highly-proliferative cancer cells (yellow arrow), *TFF1* and *CLDN4* were highly expressed. *ITGB6* and *FAP* expression was elevated to a lesser extent in the tumor, yet on the scale of spatial transcriptomic imaging was not enhanced near the ducts (Fig. 3A). Mapping of insulin (*INS*) expression provides an alternative view of the functional islets with *INS* expression and was typically enhanced in spots that do not express the cancer surface markers.

Fig. 3 | Spatial gene expression maps in PDAC and IPMN. A Spatial gene expression maps of *S100P, MUC5AC, TFF1, CLDN4, ITGB6, INS* and *FAP* in PDAC from multiple fields in a representative patient. The H&E slides in the first column illustrate the specific location of the spatial gene expression slice on the excised tissue. Yellow arrows indicate ducts. **B** Spatial gene expression levels of *S100P, MUC5AC, TFF1, CLDN4, ITGB6, INS* and *FAP* in IPMN (tissue samples from 3 patients). **C** IHC of MUC5AC and CLDN4 protein for four tissue samples (one PDAC and three IPMN). Spatial gene expression maps were based on a log-normalized gene counts using Seurat's SCTransform function, and the scale bar represents the log-normalized counts. Representative histology and gene expression maps were based on a sample replicate of 12 separate regions from large biopsy samples from 4 individual patients.

In IPMN samples, *CLDN4* expression was enhanced in high-grade lesions

By comparison, within the IPMNs (Fig. 3B), expression of *MUC5AC* and *TFF1* was greatly enhanced with a variable level of expression of *CLDN4* and *ITGB6*. *MUC5AC* expression was extensive in IPMNs, whereas *CLDN4* was preferentially enhanced in PDAC (Fig. 3A).

Immunohistochemistry (IHC) for MUC5AC and CLDN4 confirmed that their protein expression patterns were closely correlated with their mRNA expression (Fig. 3C).

In IPMN lesions (Fig. 4A–D), cancer surfaceome genes were elevated in Clusters 6, 9, 12 and 16, with a greater fraction enhanced in Cluster 12 (Fig. 4E–F). *NKX6-2*[23] mRNA counts averaged 0.002 across all
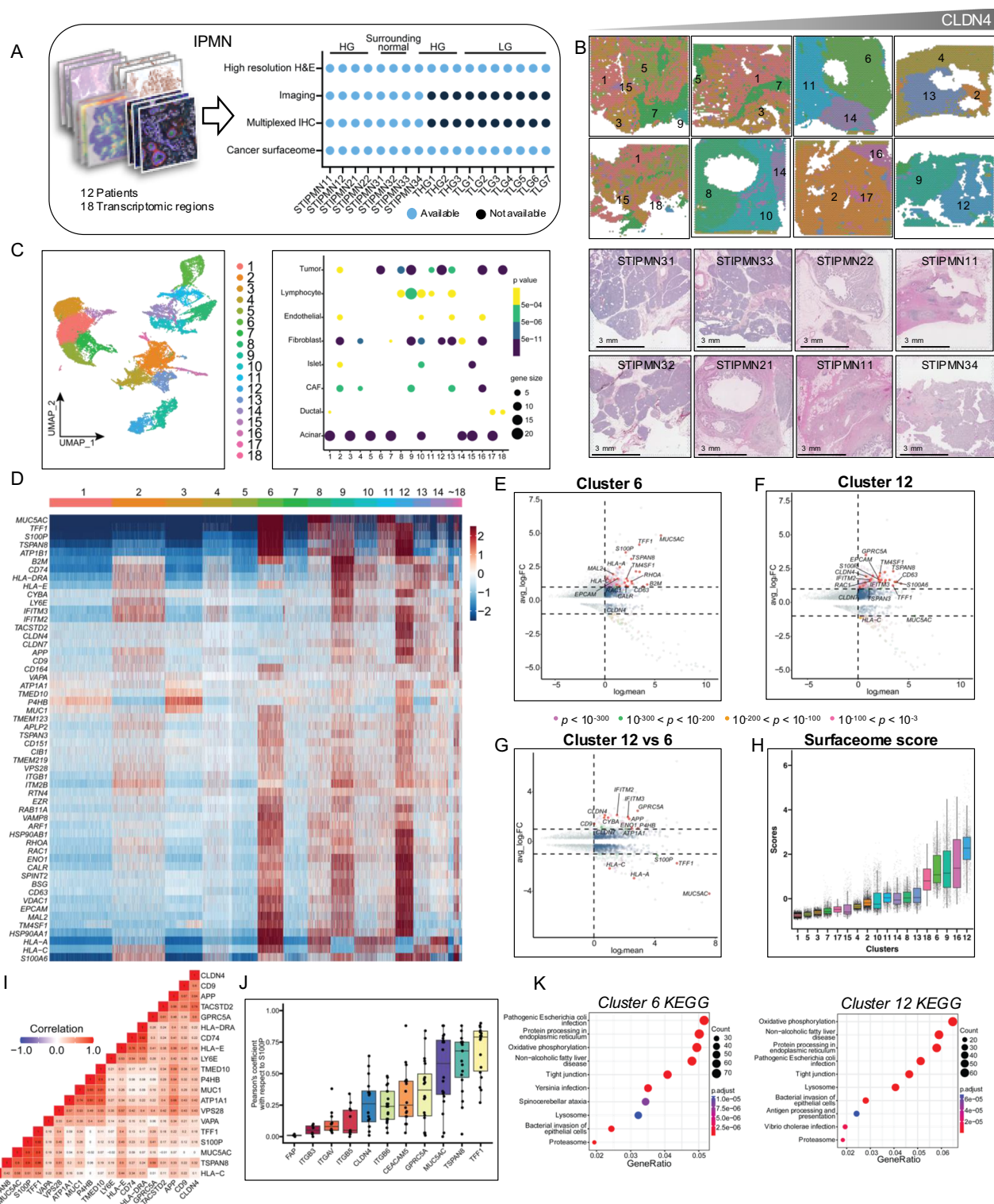
Stanford IPMN samples except for STIPMN31 (average of 1.7). When compared with underlying histology, Clusters 6 and 12 were spatially correlated with elongated ducts and hyperplastic islets. We further explored Clusters 6 and 12 by differential expression analysis. Cluster 12 included elevated expression of *CLDN4* and *GPRC5A* (Fig. 4F–G) whereas in Cluster 6, mucin producing genes, such as *MUC5AC*, were elevated. Hypergeometric t tests of differentially-expressed genes with respect to single-cell RNA cell type signatures[24,25] indicated that Clusters 6, 9, 12 and 16 were enriched in tumor signature genes with *p* values of less than 5×10^{-11}.

CNV analysis indicated that Clusters 6 and 12 had higher CNV gains (Supplementary Fig. 3A). Single-cell RNA tumor signatures in IPMN samples confirmed that tumor signature gene clusters were upregulated in Cluster 6 and 12 (Supplementary Fig. 3B). The cancer surfaceome score increased gradually across the clusters (Fig. 4H), reaching a mean score in Cluster 12 that is similar to the score observed in PDAC clusters.

In the IPMN lesions, the spatial correlation of the surfaceome markers included two groups with high inter-marker correlation, including *TSPAN8, MUC5AC, S100P* and *TFF1* in one group (> 0.9), and

Fig. 4 | Spatial transcriptomic characterization of human IPMN tissue slices.
A Summary of the IPMN study. **B** H&E slices of IPMN tumor excised from three
patients (bottom two rows) and their corresponding spatial transcriptomic spots
(top two rows) arranged based on increasing *CLDN4* expression. The spatial tran-
scriptomes between the IPMN slices were merged, clustered, and projected on the
Uniform Manifold Approximation and Projection (UMAP) dimension in (**C**) and
projected to their H&E slices. Scale bar = 3 mm. **C** Leiden clustering of IPMN tran-
scriptome projected on UMAP space. Dot plot of one-sided hypergeometric t test
results of all clusters in IPMN based on cell type signatures. **D** Heatmap of Leiden
clusters with genes selected from the PDAC cell surfaceome atlas with greater than
80% expression across sequenced PDAC cells. Scale represents z-score of log-
normalized gene counts. **E**–**G** Differential expression of Cluster 6 (**E**) and Cluster 12
(**F**) versus all remaining clusters and **G**) Cluster 12 versus Cluster 6. **H** Cancer

surfaceome score based on average normalized and scaled gene expression of all
cells and all cancer cell surfaceome PDAC genes in each cluster. **I** Pearson's cor-
relation similarity matrix of select cancer cell surfaceome genes based on the IPMN
spatial transcriptome. **J** Pearson's correlation of all spots for *S100P* vs key markers
of interest. **K** KEGG pathway enrichment of Cluster 6 and Cluster 12. Each calcu-
lation is based on $n = 18$ samples. For box plots, the center is the median and the
lower and upper bound of the box are 25% and 75% of the distribution, respectively.
The lower whisker is the lower 25% − 1.5 x interquartile range (IQR). The upper
whisker is the upper 75% + 1.5 x IQR. Differential expression analysis in (**E**), (**F**) and
(**G**) were based on non-parametric Wilcoxon rank sum test, which is a default
setting in Seurat's FindMarkers function. Gene enrichment analysis in (**K**) was done
with hypergeometric t test based on clusterProfiler package. Source data are pro-
vided as a Source Data file.

CLDN4, CD9 and *APP* in a second group (> 0.6) (Fig. 4I). *TFF1* has the
highest correlation with *S100P* of all markers in the IPMNs (Fig. 4J),
with greater variability in the PDAC markers from Fig. 1, resulting from
the range of phenotypes from normal tissue to invasive cancer
observed within the cluster. *CLDN4* expression correlates spatially with
cancer markers such as *S100P* and *TFF1*. Across the IPMN fields, Cluster
6 and 12 were both enriched in tight junction and infection-related
pathways on KEGG enrichment analysis (Fig. 4K).

Standard medical imaging of these cases with computed tomo-
graphy (CT) or magnetic resonance imaging (MRI) was also obtained
and adds support for the need for molecular imaging to characterize
lesions (Supplementary Fig. 4A–F). For example, retrospective analysis
of contrast-enhanced MRI of the CLDN4+ region in lesion STIPMN34
corresponding to Cluster 12 suggested that the lesion was suspicious
for cancer based on contrast enhancement (Supplementary Fig. 4G–J).
This suggests that molecular imaging can enhance the detection of
small regions with cancerous phenotypes.

Network analysis
We performed network analysis using the Ingenuity Pathway Analysis
program (Qiagen, CA) to assess the expression of genes that are known
to be upstream of *S100P* and *CLDN4* in PDAC and IPMN lesions using
our transcriptomic data (Supplementary Fig. 5A). In each case, *STAT3* is
known to be a part of the expression network, and *STAT3* expression is
enhanced. In addition, we found that enhanced *BMP4, NR3C1, ESR1,
PGR* and *CDK5* expression impact the expression of S100P, whereas
ERBB2, TGFB1, WNT5A and *KRAS* impact the expression of *CLDN4*. The
relative expression of these genes in Cluster 1 of PDAC samples versus
normal tissue and the IPMN Cluster 6 and 12 versus all clusters within
the IPMN samples are summarized (Supplementary Fig. 5A). Therefore,
while the spatial distribution of enhanced expression is similar for
these genes, there are differences in pathway expression, particularly in
regions in which the expression level remains low. *MUC5AC* expression
was also enhanced, particularly in early IPMN lesions. An important
upstream gene involved in *MUC5AC* expression is *IL17RA*, where the
IL17 pathway is known to be an important component of pancreatic
cancer development. (Supplementary Fig. 5B)[31]. Evaluation of IL-17
signaling in early pancreatic disease could be further probed in
future work.

CLDN4 increased at the pseudotime value associated with inva-
sive disease on pseudotime analysis
Through pseudotime analysis of an epithelial-only dataset including
normal pancreas and IPMN and PDAC regions, we then explored two
trajectories which outline IPMN and PDAC sample types. In IPMN, the
pseudotime trajectory involved an acinar-ductal transition that pro-
gressed to either IPMN or PDAC (Fig. 5A, B). By contrast, in the PDAC
clusters, acinar-ductal metaplastic clusters rapidly progress to PDAC.
When we further remapped the pseudotime trajectory into the spatial
dimension on a unified scale, regions with a cancer-like or normal
phenotype were segmented in IPMN (Fig. 5C–D). In PDAC, we found

that ductal-originated cancerous cells were scattered throughout the
specimen (Fig. 5E).

The IPMNs highly expressed *MUC5AC* and *TFF1* at earlier pseu-
dotime values, with *MUC5AC* expression decreasing over time
(Fig. 5F-G). Alternatively, *CLDN4* increased at the pseudotime value
associated with invasive disease (Fig. 5F-G), confirming the results
from Fig. 4G-H, which also demonstrated that *CLDN4* was enhanced in
the IPMN region with the highest cancer surfaceome score.

The enhanced expression of *CLDN4, TSPAN8* and *TFF1* on cancer
cells was not significantly reduced after treatment with chemotherapy
with or without radiation (Fig. 5H-I). To explore whether *CLDN4* can
differentiate PDAC from normal pancreas and precancer, we com-
bined samples from our site with refs. 24–26, which included normal
pancreas, and IPMN and PDAC samples. Regions were constructed
from multiple spots with similar expression levels (e.g. lower 20% or
upper 20% of expression levels) and classified. The area under the
curve (AUC) for the differentiation of PDAC from normal or pre-
cancerous tissue for *CLDN4, S100P, MUC5AC, TFF1, CEACAM5,* and
TSPAN8 was 0.9, 0.5, 0.3, 0.5, 0.8, and 0.4, respectively (Fig. 5J).

Finally, we analyzed subclusters of the cancer-associated Cluster
1 in Fig. 1 (Supplementary Fig. 6) in order to characterize the pheno-
type of spots without *CLDN4* overexpression. Unsupervised clustering
of cluster 1 from PDAC samples distinguished 10 subclusters (Sup-
plementary Fig. 6A), and *CLDN4* expression was not enhanced in
Subcluster 10 (Supplementary Fig. 6B). Differential expression ana-
lysis demonstrated enhanced expression of *TFF2, MUC6, LYZ, NKX6-2,
PGC, GKN2, VSIG1, CXCL17, CLDN18* and *GOLM1* in this subcluster
(Supplementary Table 5 and Supplementary Fig. 6C). A fraction of
these spots had a high Pearson spatial correlation between *TFF2,
MUC6* and *LYZ* overexpression, corresponding to mucous neck cells
or antral gland cells[32] (Supplementary Table 5 and Supplementary
Fig. 6D). In addition, in a fraction of spots, *NKX6-2, PGC, GKN2, VSIG1,
CXCL17* and *GOLM1* expression was spatially correlated with a Pearson
correlation greater than 0.4 (Supplementary Fig. 6D). Overexpressed
genes in each of these correlated regions were enhanced earlier in
pseudotime as compared with *CLDN4* (Fig. 5F, Supplementary
Fig. 6E), suggesting that these spots correspond to a lower-grade
phenotype.

Activated fibroblasts were organized in thin layers surrounding
high-grade lesions
We then performed 51-plex CODEX and IHC (Fig. 6A). With enhanced
single cell resolution, ductal lobules on the order of tens of microns
can be visualized and the phenotype determined (Supplementary
Fig. 7). In regions harboring high numbers of high-grade PanINs (large
CD66+ ductal features) (Fig. 6B), CD45+ immune infiltration, acinar-to-
ductal metaplasia (ADM, indicated by small Keratin8/18hiEpCAM+
ductal features), and overall loss of acinar structure (EpCAM+ epithelial
cells) was observed. Importantly, thin bands of fibroblasts (a-
SMA+Podoplanin+ cancer associated myofibroblasts (myCAFs)) selec-
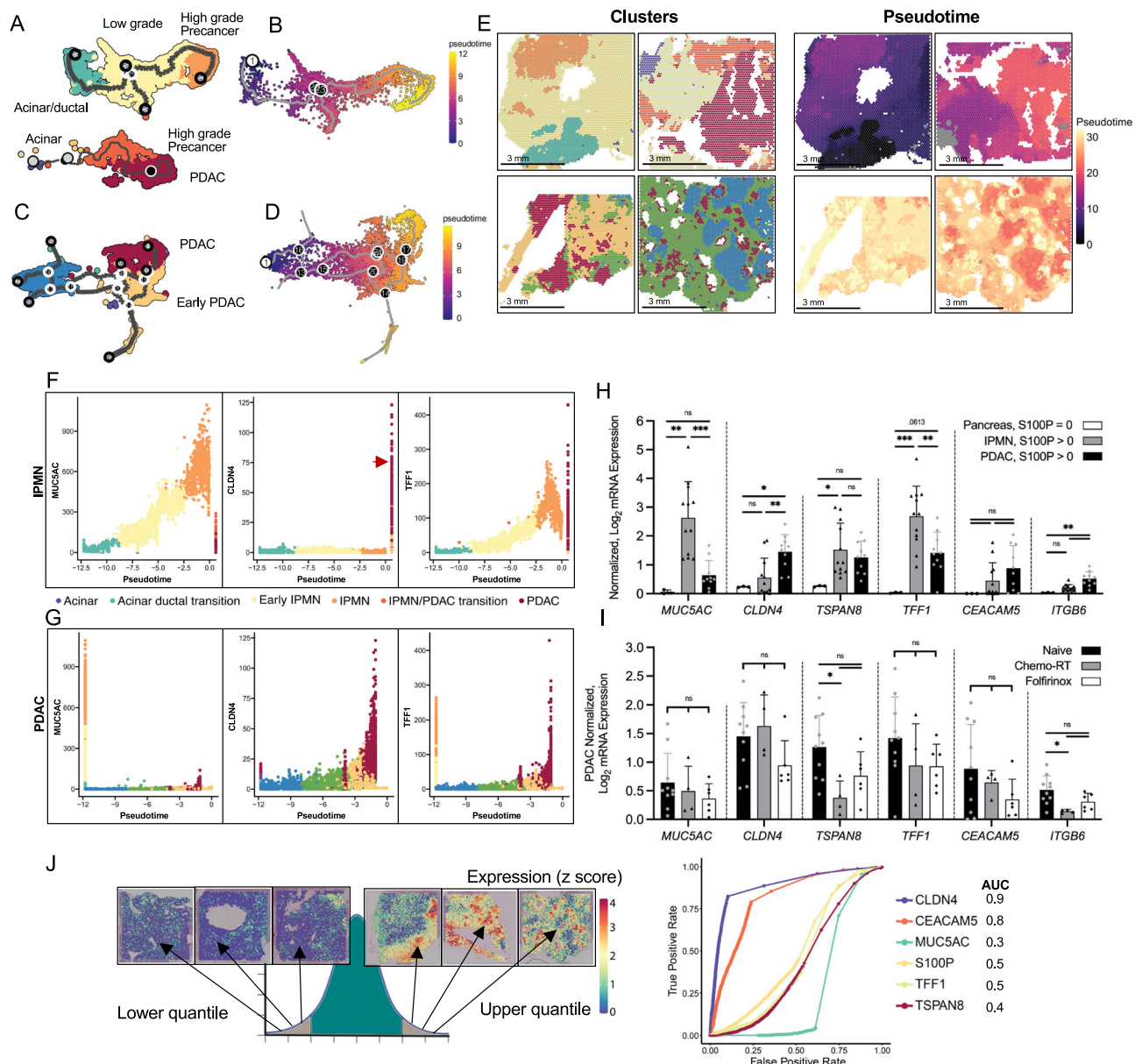tively stratified high-grade PanINs (Fig. 6B).

Fig. 5 | Pseudotime analysis of PDAC and IPMN human tissue spatial transcriptomes. A Annotated spot population of clusters containing acinar ductal transition that progressed to IPMN. B Pseudotime trajectory of acinar ductal transition to IPMN in (A). C Annotated spot population of clusters containing acinar ductal transition to PDAC. D Pseudotime trajectory of acinar ductal transition to PDAC spots in (C). Scale bar represents pseudotime. E Spot clusters projected on their corresponding histology slices and the pseudotime trajectory values projected into the spatial dimension. Scale bar represents pseudotime. F–G *MUC5AC, CLDN4* and *TFF1* expression levels with respect to pseudotime in (F) IPMN and (G) PDAC, based on a pseudotime scale where 0 is invasive cancer (red arrow). H Spots with normalized log base 2 expression of *MUC5AC, CLDN4, TSPAN8, TFF1, CEACAM5* and *ITGB6*, based on co-expression levels of *S100P* in surrounding pancreas (normal tissue), and IPMN and PDAC tissue. ns = not significant. I Spots with identical genes and expression level based on co-expression levels of *S100P* in naïve PDAC tissue, PDAC tissue from patients treated with chemotherapy and radiation therapy (Chemo-RT), and PDAC tissue from patients treated with the chemotherapy Folforinox. J Receiver operating curve (ROC) obtained from mRNA spatial analysis of all PDAC and IPMN samples for surfaceome genes. Statistics were analyzed with one-way ANOVA for each column, * = $p < 0.05$, ** = $P < 0.005$, *** = $P < 0.0005$, **** = $p < 0.00005$ unless otherwise stated and the whiskers represent standard deviation. Source data are provided as a Source Data file.

To further classify individual cell phenotypes, we performed unsupervised clustering to generate 18 independent populations which were then manually annotated based on canonical expression profiles (Fig. 6C). Fibroblasts were segmented into a-SMA⁺Podoplanin⁺ myCAFs and a second population of heterogenous fibroblasts (a-SMA^lo^Podoplanin^lo^) (Fig. 6C). As a result, we further explored CAF phenotype signatures in the transcriptomic data within PDAC and IPMN samples. We removed tumor and immune cells with low *VIM* and high *EPCAM* expression or high *PTPRC* expression. Using myCAF and iCAF signatures compiled from[33–35], key myCAF genes were expressed

in PDAC samples to a greater extent than iCAF genes (Supplementary Fig. 8A-B). In the IPMN samples, myCAF genes were expressed in all clusters and to a greater extent in Cluster 9 and 17 (Supplementary Fig. 8C). Expression of iCAF gene signatures was low (Supplementary Fig. 8D).

By extracting Acinar, myCAF, High-Grade PanIN, and Low-Grade PanIN/ADM populations as annotated in Fig. 6C, we found across all CODEX regions that ducts surrounded by myCAFs contained highly-proliferative tumor cells (Fig. 6D). These findings were validated by calculating the likelihood, or strength, of cell-cell pairwise interactions
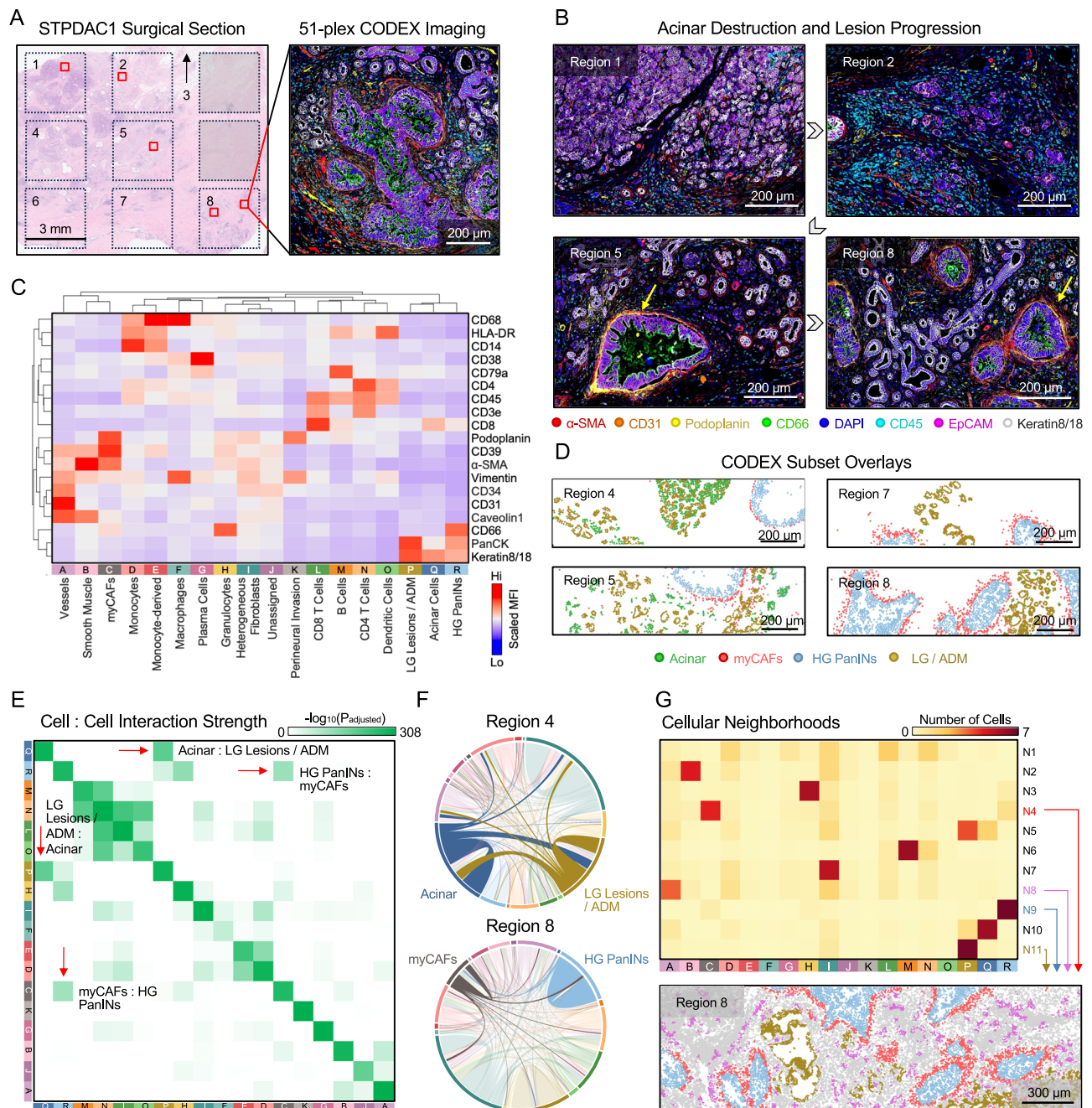
Fig. 6 | Mapping of protein at single-cell level in PDAC. A 10 regions obtained from a single PDAC surgical section were stained with H&E and a 51-plex CODEX panel. Region 3 is above the boundary (not pictured) while the two shaded regions were not analyzed due to poor cell quality. B Representative CODEX images depicting acinar destruction, immune infiltration, and myCAF stratification in regions with increasingly severe levels of disease progression (grey arrows). Fibroblasts encompassing cancerous duct are shown with yellow arrows. C Scaled expression heatmap for all 8 analyzed regions across 18 manually annotated cell clusters (generated via unsupervised Leiden clustering). D "Acinar", "myCAF", "High-grade (HG) PanINs", and "Low-grade (LG) Lesions / ADM" populations were

plotted across four regions, highlighting discrete organization. E Cell-cell interactions (pairwise adjacency, knn = 10) were quantified and averaged for all 8 regions across the 18 clusters, and select interactions are marked with red arrows. F Chord diagrams of regions 4 and 8 highlight heterogeneity in the frequency of cell-cell interactions (width of chord) and individual populations (length of arc). G 11 cellular neighborhoods, each composed of 10 cells, were generated for the entire CODEX dataset with representative spatial organization shown for Region 8. All calculations were done with n = 7 individual regions. Source data are provided as a Source Data file.

for all regions, showing that acinar cells were likely to interact with ADM, and myCAFs, with high-grade PanINs (Fig. 6E). We further visualized these cell-cell contacts using chord diagrams, emphasizing the connection of myCAFs and high-grade PanINs (Fig. 6F).

High-grade PanIN cells and myCAFs each comprised unique neighborhoods that were well-defined and co-localized spatially (Fig. 6G, Neighborhoods 9 and 4, respectively). Early lesion cells, ADM,

and acinar cells were grouped together into neighborhood 5, supporting the cell-cell interaction results from Fig. 6H and likely representing areas of tissue where early pancreatic oncogenesis is present. Neighborhood 8 was built primarily of CD31+Caveolin1hi endothelial cells and a few heterogeneous CAFs (stellate cells are likely found in this cluster), reflecting angiogenic neo vessels distributed across the tumor landscape.

As previously shown in Fig. 2B, high-grade PanINs expressed elevated *CLDN4* across and within the duct. CODEX results indicate that myCAFs were organized in thin layers surrounding the high-grade lesions. The spatial localization of these neighborhoods further illustrates the cellular components that promote PDAC oncogenesis and motivates the selection of *CLDN4* as an imaging and therapy target[36].

TLOs and sparse immune infiltrates reveal leukocyte heterogeneity

As we considered possible molecular-imaging strategies, we also assessed the distribution of immune cells within PDAC and precancers. In both PDAC and IPMN transcriptomic samples, the spatial correlation (Pearson's coefficient) between epithelial cell markers and typical immune receptors (CD3, CD8, CD64 *(FCGR1A)*, CD14) was nearly zero (Supplementary Fig. 9A, B). Both proliferation (Ki67) and immune cell density were enhanced in the IPMN center (Supplementary Fig. 10A-D). Immune cell density was heterogeneous due to the presence of both TLOs and scattered individual leukocytes. TLOs were distributed throughout IPMNs/PDACs and detectable on spatial transcriptomics due to their millimeter-scale, spherical/oblong morphology and intense expression of immune-related genes (Supplementary Fig. 11A, B). TLO differentially-expressed genes (DEGs) and associated pathways were enriched for B/T cells, B-cell receptor/T-cell receptor (BCR/TCR) signaling, chemokine/cytokine interactions, immune cell activation, proliferation and differentiation (Supplementary Fig. 11C-F). The spatial organization of these structures was well-defined, as T cells (CD4 and CD8), B cells (CD20 and CD21), dendritic cells (CD141), plasma cells (CD38) and high endothelial vessels (CD31) were shown to occupy specialized zones within TLOs (Supplementary Fig. 11G). Upon filtering the CODEX TLO data for T and B cells, we also found that CD45RO and CD44 were highly co-expressed on both CD4 and CD8 T cells, indicative of an activated memory phenotype (Supplementary Fig. 11H, I). Furthermore, Ki67 was primarily found on TLO-core B cells (Supplementary Fig. 11H, I).

Within the IPMNs (Supplementary Fig. 12A–D), lymphoid structures were frequent; however, these structures often lacked the organization demonstrated in mature TLOs (Supplementary Fig. 12A, B). We then quantified the leukocyte frequency and phenotype across the IPMN and treatment-naïve PDAC regions (Supplementary Fig. 12C, D). Leukocyte frequency increased in both IPMN and PDAC tissues compared with the surrounding normal pancreas (Supplementary Fig. 12C). The high immune cell variability in the IPMN results from a wide range of immune infiltration (20 to 60% of total cells) within each acquired CODEX region (Supplementary Fig. 12C).

## Results point to biologically-driven molecular imaging of CLDN4

Based on our spatial multi-omic analyses, CLDN4 emerged as an imaging and potential therapeutic target due to its high differential expression between high-grade lesions and normal tissues, consistent correlation across mRNA expression with other cancer markers such as *S100P* and late-stage expression in pseudotime. Small peptides are superior for targeting due to the ease of synthesis, comparable potential affinity and specificity, improved pharmacokinetic profiles, and low immunogenicity. *Clostridium perfringens* enterotoxin (Cpe), a natural ligand to CLDN4, is 35 kDa. The C-terminus of Cpe (cCpe), a truncated form of Cpe, binds to the extracellular segments of CLDN4 with a reported nanomolar binding affinity constant (K_D)[37]. Several short peptides that bind to the ECL4 loop in CLDN4 have been identified[38]. Our ligand validation through a docking simulation with human CLDN4 (Supplementary Fig. 13A) suggests that Cpe30 MT2 (NSSYSGNYYSIL, with a reported K_D of 1.97 nM, sequence will be abbreviated hereafter to C4BP (claudin-4 binding peptide)) is promising for human imaging. We therefore synthesized DOTA-PEG$_2$-C4BP on a rink amide resin using a microwave-assisted peptide synthesizer. DOTA, a ^{64}Cu chelator, which also incorporates various therapeutic and diagnostic metal isotopes, was attached after one PEG spacer unit to avoid steric hindrance (Supplementary Fig. 13B). High-performance liquid chromatography (HPLC) purification afforded DOTA-PEG$_2$-C4BP in >95% purity with exact mass (M + H$^+$, calculated 1897.9 Da, found 1898.0 Da) as confirmed with matrix-assisted laser desorption/ionization (MALDI) mass spectrometry (Supplementary methods and Fig. 13C). The radiolabeling of DOTA-PEG$_2$-C4BP (2 nmol) with ^{64}CuCl$_2$ (70 MBq) conferred ^{64}Cu-DOTA-PEG$_2$-C4BP (28 MBq/nmol, ^{64}Cu labelled DOTA-PEG$_2$-C4BP will be abbreviated to ^{64}Cu-C4BP hereafter) in 80% non-decay corrected yield with >99% radiochemical purity (Supplementary Fig. 13D).

Imaging of *Kras*$^{LSL-G12D/+}$;*Trp53*$^{fl/fl}$;*Rosa26*$^{LSL-tdTomato/LSL-tdTomato}$;*Ptf1a*^{CreER} (KPTC) mice, in which PDAC is driven from acinar cells in adult mice after tamoxifen treatment, was then performed at 49, 84, and 120 days after tamoxifen injection (Fig. 7A), which was near the average survival duration[39]. Importantly, to mimic human PDAC development which occurs in adults, mice were aged to adulthood (8 – 10 weeks) before tamoxifen introduction. Pancreatic tumors and multi-organ metastases occur after tamoxifen treatment. In this model, substantial CLDN4 protein expression was detected in pancreatic tumors and metastases (Fig. 7B). At 49 days post tamoxifen treatment, a dynamic PET/CT scan was simultaneously acquired with tail vein administration of ^{64}Cu-C4BP ($n = 4$, ~0.1 µg/mouse), and imaging in the 25-30 minute window displayed a significant retention of radiolabeled ligand at the tumor sites in this transgenic mouse model (white arrowheads, Fig. 7C). Tumors and metastases were observed in three-dimensional maximum intensity projection (MIP) images (Supplementary Movies 1-4, white and yellow arrows indicate tumors) and slice images in cancer-burdened mice and not in wild-type animals (Fig. 7C-D). H&E and CLDN4 IHC stains of the intestine and liver showed metastases that aligned with the PET imaging results (Supplementary Fig. 14A-C).

Image-based quantification assessed the accumulation of injected activity per cc (%IA/cc) in the tumor and blood, peaking at ~15%IA/cc (2 min) and clearing to < 5%IA/cc (30 min), respectively, in tumor-burdened mice 49 days after tamoxifen administration (Fig. 7E). At later tamoxifen time points, accumulation had increased to ~25%IA/cc in metastases and was retained at ~18%IA/cc in the pancreas within 30 minutes after ^{64}Cu-C4BP injection (Fig. 7F). Since MRI provides more detailed soft tissue anatomical reference than CT and the KPTC mouse model has been shown to have increased signal intensity at the tumor location in T2-weighted MRI, we performed multi-modal imaging including T2-weighted MRI, PET/CT, and bright field imaging to validate that the region retaining ^{64}Cu-C4BP signal was consistent with pancreatic cancer (Fig. 7G). Ex vivo PET imaging confirmed the localized accumulation of ^{64}Cu-C4BP within the colon, pancreas and liver in transgenic mice (Fig. 7H). Biodistribution showed 6.6 ± 3.9%IA/g in the kidneys and 7.7 ± 5.4%IA/g in the liver at 22 h post injection (Supplementary Table 4). Additionally, the pancreas-to-muscle ratio in transgenic mice (3.71 ± 0.56%IA/g, $p = 0.003$) was significantly higher than age-matched wild-type mice (1.53 ± 0.1%IA/g) (Supplementary Table 4).

We then repeated the imaging study in the Capan-1 xenograft mouse model, once tumors reached 5-10 mm (Supplementary Fig. 15). The Capan-1 mouse model expresses human CLDN4 (Supplementary Fig. 15A, B), as human CLDN4 is highly conserved as compared to mouse protein. Accumulation was verified by PET MIP and slice imaging at 30-60 minutes after injection (Supplementary Fig. 15C, D), with retention of ^{64}Cu-C4BP detected in the tumor (indicated by white arrowheads). The spatial map of the radioactivity and CLDN4 expression obtained from PET and IHC tumor images confirmed colocalization of CLDN4 and ^{64}Cu-C4BP (Supplementary Fig. 15E). Maximum tumor accumulation reached ~12%IA/cc at 2 minutes and was retained at 6% after 60 minutes (Supplementary Fig. 15F). Blood activity was reduced over 60 min with the radiopharmaceutical clearing through the kidney (Supplementary Fig. 15G, H). A blocking study achieved by
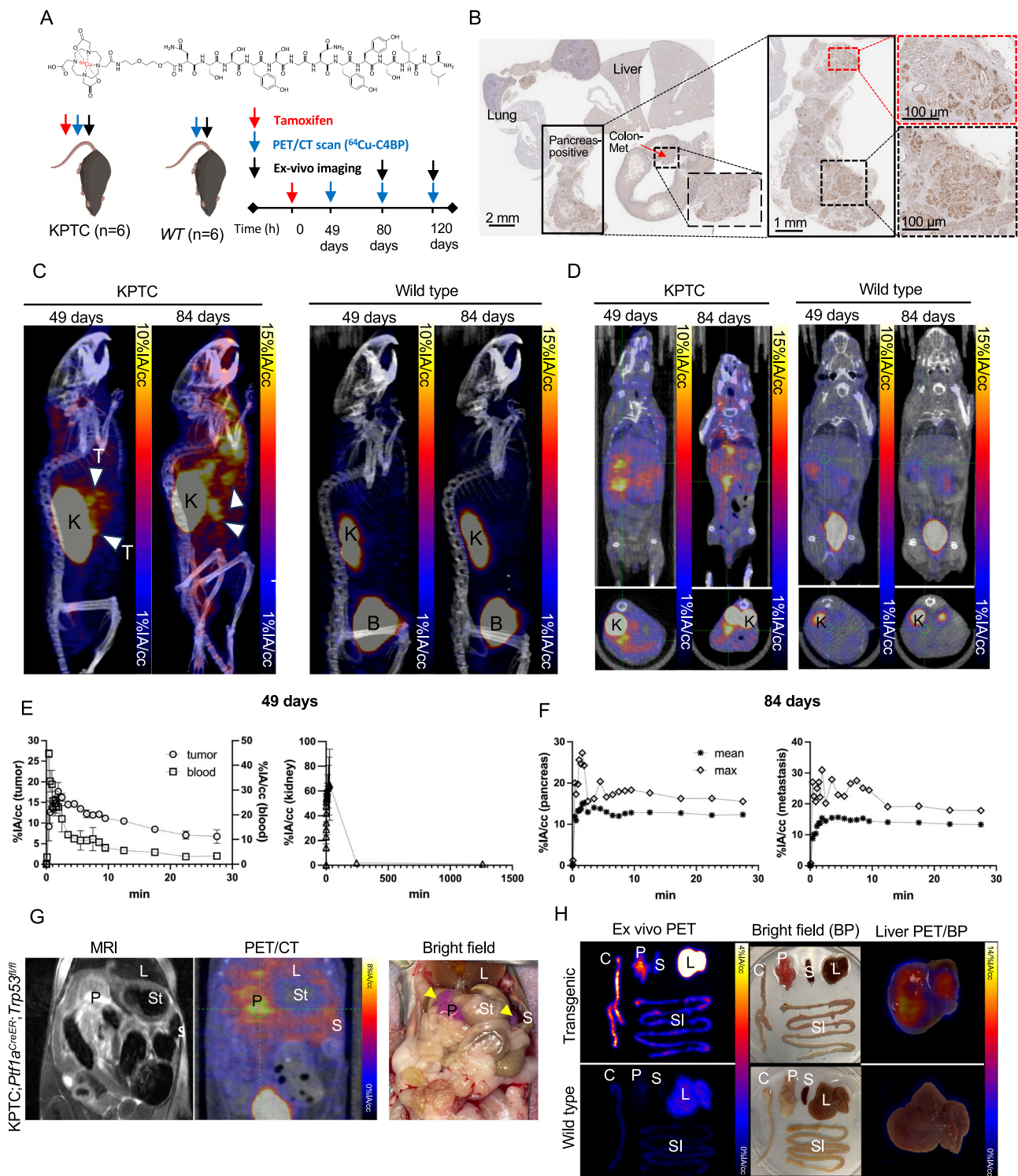
co-injection of a 500-fold excess of the cold compound reduced ^{64}Cu-C4BP accumulation in the tumor by 35% ($p = 0.009$) (Supplementary Fig. 15G). Biodistribution of ^{64}Cu-C4BP acquired at 2.5 h post injection showed a 48% decrease in radioactivity in the blocked group ($1.21 \pm 0.64\%$IA/g, $p < 0.001$) over the unblocked group ($2.31 \pm 0.23\%$IA/g) (Supplementary Fig. 15I).

Lastly, we explored the spatial extent of a therapeutic radiation dose delivered to the human surgical sample lesions, assuming that a therapeutic radiopharmaceutical successfully bound in a manner proportional to the local mRNA concentration (Supplementary

Fig. 16). We compared the distribution of *CLDN4* and *MUC5AC* mRNA to that of *S100P* as the gold standard (Supplementary Fig. 16A), where red spots would represent regions with *S100P* above baseline but in the absence of the CLDN4 or MUC5AC targeted drug. We found that nearly all of the 100 μm spots which express *S100P* also express *CLDN4* (Supplementary Fig. 16A, B). Furthermore, given the effective therapeutic range of alpha or beta emitters (Supplementary Fig. 16C, D), few voxels, if any, would be excluded from a therapeutic dose using a CLDN4-targeted radiopharmaceutical. This finding will be assessed in vivo in future work.

Fig. 7 | Molecular imaging of claudin-4 (CLDN4) in a PDAC mouse model.
A CLDN4-binding peptide and imaging scheme for study in tamoxifen-induced pancreatic cancer in the $KPTC$:$Kras^{LSL-G12D/+}$;$Trp53^{fl/fl}$;$Rosa26^{LSL-tdTomato/LSL-tdTomato}$;$Ptf1a^{CreER}$ mouse model of PDAC ($n = 6$). Mice created with BioRender.com. **B** CLDN4 immunohistochemistry of organs (liver, lung, colon and pancreas) from the tamoxifen-induced PDAC mouse model. We used ^{64}Cu-C4BP and demonstrated tumor-specific accumulation. This transgenic model expresses CLDN4 in both the pancreatic lesions and metastases (Met) after tumor induction. Representative image based on $n = 6$ mice with similar expression levels. **C** PET/CT maximum intensity projection (MIP) images acquired in the first 30 minutes after ^{64}Cu-C4BP injection in the transgenic mouse model at 49 or 84 days after tamoxifen treatment. White arrowheads indicate accumulation of ^{64}Cu-C4BP at the tumor sites. In the wild type mouse, ^{64}Cu-C4BP is visible only in the clearance organs (kidney and bladder). **D** PET/CT slice images showing retention of ^{64}Cu-C4BP within the pancreas (crosshair). **E** Time-activity curves (TACs) for blood, tumor, and kidney at 49 days

(note that ^{64}Cu-C4BP clears from the kidney). 2 ROIs per mouse were used to calculate intensity with a mouse sample of $n = 6$. **F** TACs for the pancreas and metastases at 84 days. G) Magnetic resonance imaging (MRI), PET/CT, and bright field images of abdominal region from the same mouse at 120 days after tamoxifen treatment. ^{64}Cu-C4BP in the PET/CT image is well localized to the pancreatic lesion in the MRI and bright field images. Yellow arrowheads denote tdTomato signal (i.e. tumor lesions) in the bright field image in (**G**). **H** In the same model at ~84 days after tamoxifen treatment, ex vivo PET imaging with ^{64}Cu-C4BP detects disease in the pancreas, colon and liver. Tumor cells express tdTomato in this model producing a red hue in the pancreas and colon. In this transgenic cancer model, liver accumulation is high and associated with metastasis. A small amount of activity accumulates in the liver due to clearance in the wild-type (WT) mouse. Graphs are presented as mean ± s.e.m. Abbreviations: L: liver, P: pancreas, St: stomach, S: spleen, C: colon, SI: small intestine, K: kidney, B: bladder, T: tumor. Source data are provided as a Source Data file.

Discussion

The development of biologically-inspired strategies to image and treat cancers with precise molecular targeting has high significance. With the emergence of spatial methods and data sets, there is an opportunity to use molecular imaging both to detect cancer and to design and implement therapeutic strategies. Here, we applied spatial multi-omics techniques to characterize the distribution of cancer cell surface markers in order to design an imaging and theranostic strategy. We created a cancer surfaceome score and found that high scores were spatially correlated with a cellular morphology consistent with cancer.

Most importantly, we found that the expression of a small number of tumor surface markers, including *CLDN4*, was consistent across the patients studied, with less variability than integrin, fibroblast or immune cell markers. In the cancer cluster, the expression of genes encoding surface markers *CLDN4*, *GPRC5A*, *TSPAN8*, and *CEACAM5* was enhanced more than 13-fold compared with the normal pancreas, whereas *FAP* and *ITGB6* were differentially expressed by less than 4-fold. *CLDN4* was expressed on ~88.8% of PDAC cells in ref. 11, and here we found that ~89% of spots in the cancer-associated cluster expressed elevated *CLDN4*. The fraction of spots overexpressing CLDN4 increased to 97.5% upon integration (as compared with merging) of the data, reflecting differences in the sequencing depth at different sites. Such differences should be further analyzed in the future. Receiver operating characteristic analysis of PDAC diagnosis based on the top surface markers indicated that the area under the curve (AUC) was greatest for *CLDN4* (~ 0.9).

Enhanced *CLDN4* expression and localization in regions of invasive cancer were consistent throughout PDAC lesions whether treatment naïve or post therapy. *CLDN4* expression increased later in the transition to invasive cancer than *MUC5AC* or *TFF1*, suggesting that this marker may differentiate between premalignant and invasive lesions. A retrospective evaluation of contrast MRI imaging suggested that molecular imaging of CLDN4 could have been useful in detecting a region with a high cancer surfaceome score. Based on the analysis of IPMN lesions in ref. 23, in spots with minimal *NKX6-2* expression, *CLDN4*, *CXCL2*, *CD74*, *LY6E*, and *SPP1* expression was greater and was associated with PDAC progression and neoplastic progression of IPMN[23,40]. *NKX6-2* expression was low in our cancer cluster, and the results support our pseudotime analysis and solidify *CLDN4* as a marker to differentiate high- and low-grade lesions.

The resulting PET imaging approach demonstrated exquisite sensitivity for the detection and mapping of small tumors and metastases in mouse models with molecularly-specific accumulation. While *CLND4* is expressed in the normal colon, here, we found that the resulting radiopharmaceutical accumulation in normal tissue was low, likely due to the expression of this target in cell-cell junctions. Accumulation of the CLDN4-targeted peptide reached ~25%ID/cc in metastases and ~18% IA/cc in the pancreas at 30 minutes after ^{64}Cu-

C4BP injection. Preclinical single photon emission computed tomography (SPECT) imaging of CLDN4 has been explored with an antibody[41] and other peptides in the past[42]; however, our ligand enhanced accumulation and improved signal-to-noise ratio. For imaging of integrins, $\alpha_v\beta_6$ has been the most promising with affinity of < 55 nM and uptake of ~2–4%ID/cc in a pancreatic cancer xenograft[43] or affinity of 0.047 nM and ~8% ID/cc accumulation in lung or breast cancer models[44] reported. However, our results suggest that the expression and localization of integrins on PDAC cells are lower than that of *CLDN4* and are reduced by chemotherapy or chemo-radiation therapy. Due to the high specificity and accumulation in tumors and metastases, we are optimistic that this CLDN4-binding peptide will successfully detect pancreatic cancer in human studies. While small animal imaging PET scanners have high sensitivity, with the advent of extended field-of-view scanners, the sensitivity of clinical PET imaging is increased 10-fold from earlier work and thus the feasibility of detecting small metastases will improve. Further, in human imaging, the distance between the clearance organ (kidney) and the pancreas is increased, further improving visualization.

A single cell-based 'omic analysis is required to fully characterize the interaction of immune and fibroblast components with epithelial targets. The immune cell distribution within pancreatic lesions was complex and will likely prove challenging to harness as a cancer-specific diagnostic feature. Without adding CODEX, we would have missed the presence of thin layers of activated fibroblasts surrounding cancerous ducts due to the relative spatial resolution and sensitivity of current spatial transcriptomic methods. Still, the numbers of myCAFs near the cancerous ducts was small and targeting these cells may not be efficient for a theranostic strategy.

Peptide targeted radionuclide therapy (PTRT) is a promising strategy for PDAC and the CLDN4-targeted peptide described here shows promise to be incorporated in PTRT. We found that a beta radiopharmaceutical field generated from a CLDN4-targeted therapy would generate an approximately uniform field for the entire cancerous specimen. Systemic administration of ^{177}Lu-targeted radio-pharmaceuticals can result in specific targeting of cancer cells throughout the body and induces the cytotoxic effects of ionizing radiation[45]. PTRT has improved the overall survival of neuroendocrine tumors[46] and metastatic castration-resistant prostate cancer[47], and is approved by the FDA. A future goal of this work is to incorporate CLDN4 targeting in the treatment of PDAC. Thus, the results suggest that a data-driven target selection would result in the selection of a target such as CLDN4, and we are encouraged to find that promising affinity and accumulation are feasible.

In summary, we find that spatial transcriptomics is highly useful for the selection of molecular imaging agents. While the imaging of integrins or fibroblasts can be useful, the development of epithelial-based molecular imaging and theranostic agents is desirable. CLDN4 is

one such target, and imaging of this target with high sensitivity and specificity is feasible.

Methods

Ethics statement

All experiments and methods were performed in accordance with relevant guidelines and regulations. All animal experiments were conducted with approval from the Stanford University Administrative Panel on Laboratory Animal Care (APLAC). All studies involving human subjects were approved by the Institutional Review Board (IRB) of Stanford University and were deidentified and collected with written and signed informed consent.

Spatial transcriptomic processing and analysis

Formalin-fixed, paraffin-embedded (FFPE) human pancreatic cancer tissue sections were placed on spatial transcriptomic slides for spatial transcriptomic sequencing based on the 10x FFPE workflow (10x Genomics, Pleasanton, CA). Individually indexed libraries were sequenced on the Novaseq 6000 (Illumina Inc., San Diego, CA). Raw sequencing counts were processed through the SpaceRanger pipeline (10x Genomics) and aligned with a human reference (GRCh38). Downstream transcriptomic analysis was performed based on the Seurat framework with modifications. Spatial transcriptomic samples were merged or integrated using R function for merging and the Seurat integration function based on canonical correlation analysis. Normalization was performed with SCTransform, which minimizes technical noise such as difference in sequencing depth. Stanford-acquired data detected an average of 3706 spots per sample and 17943 aligned gene features, while PDAC datasets from HTAN[24] detected 4992 spots per sample with 36601 aligned gene features. IPMN datasets from NCBI GEO (GSE233254) detected an average of 941 spots with 36601 aligned gene features[23]. Principal component analysis was performed, and the elbow plot indicated that the first 75 principal components were sufficient to describe over 99% of the data.

To optimize for subsequent Leiden clustering parameters such as number of principal components, resolution, and number of k nearest neighbors, the average silhouette score of all clusters was used as a tuning metric to design our hyperparameter tuning grid. Based on our optimized parameters, we performed Leiden clustering and projected the clustering results on the Uniform Manifold Approximation and Projection (UMAP) dimensions. We then computed the top 10 differentially-expressed genes of each cluster compared to all the remaining clusters using Seurat's built-in functions. Since in spatial transcriptomics, each spot is not a single cell, and annotation based on cell types may not be appropriate, we performed statistical overlap calculations comparing clusters to cell signatures. Using the PDAC cell signature gene sets from single cell RNA sequencing[24,25], we performed one-sided hypergeometric t tests using differentially-expressed genes from each cluster. To plot cancer cell surfaceome gene expression levels throughout the clustered spots, we selected for surfaceome genes specific to PDAC and that are at least 80% upregulated compared to normal tissue. We further developed a cancer cell surfaceome score based on the total sum average normalized and scaled gene expression of cancer cell surfaceome in each cluster:

$$\text{cscore} = \sum_{j=1}^{S} \frac{\sum_{i=1}^{N}(g_i - \bar{g})}{\sigma} \qquad (1)$$

Where S is number of cancer cell surfaceome genes, N is total number of spots, g_i is normalized and scaled count of each gene, $\bar{g}$ is average nomalized and scaled count and σ is variance. Pearson's correlation coefficients for each spot and each sample were calculated based on the standard Pearson's correlation equation. Gene set analysis was performed with clusterProfiler enricher function in KEGG, GO, and REACTOME databases with the top 10 most significant pathways plotted[48]. Differential expression fold change values mapped onto KEGG pathway plots were further calculated with pathview function in R and then simplified to key pathways. Pseudotime trajectory analysis was performed with monocle3 on a merged dataset containing two surrounding normal tissue slices, two PDAC slices, and two IPMN slices. From our population annotations, we have identified two origins which we defined as acinar ductal transitions. Acinar-ductal cell transitions and metaplasia have been demonstrated by other groups as an important component in the development of PDAC[2]. To focus on the development from acinar-ductal transition to full cancer, we removed cancer associated fibroblasts, plasma cells, and immune cells in our trajectory. The calculated trajectories were analyzed based on their corresponding partitions in, respectively, IPMN and PDAC. To explore the spatiotemporal relationship between PDAC phenotypes, multiple pseudotime partitions were connected sequentially, and then pseudotime values were plotted with respect to their x-y spatial coordinates.

The copy number variation (CNV) calculation was performed with the infercnv package[49] with the default settings by comparing each cluster to the average of all clusters. Single-cell RNA (scRNA) tumor signatures were obtained from[24].

CODEX processing and analysis

FFPE pancreas slices were stained with a 51-plexed antibody panel as in ref. 50. After imaging processing, DAPI-based cell segmentation was performed with the DeepCell algorithm through the Enable-Medicine portal. We further filtered the segmentation results based on size of the cell, total biomarker intensity, DNA channel intensity and signal coefficient of variation using EnableMedicine's SpatialMap package on R. The filtered segmentation results were then normalized and scaled for principal component analysis. Unsupervised Leiden clustering was then executed to identify cell populations of interest. Populations were manually annotated using expression intensity patterns and spatial organization. Cell-cell interactions were calculated using a k nearest neighbors algorithm to create a graph network of individual cells (10 nearest neighbors were used), and then pairwise adjacency was calculated using a hypergeometric method. Neighborhoods were constructed using the previous calculated nearest neighbors graph (knn = 10), and k = 11 neighborhoods were built based on an optimal silhouette score. Segmented regions were also exported to the cloud-based cytometry platform OMIQ for additional visualization.

Therapeutic simulations

To model peptide binding to a given spatial transcriptomic region, we first labelled spatial transcriptomic spots using an expression threshold for *MUC5AC/CLDN4* and *S100P*. The thresholds were assigned by first selecting spots that had expression greater than 0 for *MUC5AC/CLDN4* or *S100P*, and then calculating the first quartile of expression for those genes in the corresponding positive expressing spots. Then, all spots for a spatial transcriptomic region were assigned into four groups (Gene < Threshold and *S100P* < Threshold, Gene <Threshold and *S100P* > Threshold, Gene > Threshold and *S100P* > Threshold, Gene > Threshold and *S100P* < Threshold) using the previously calculated thresholds. Dose point kernels (DPKs) were acquired for alpha/beta particle emitters (^{211}At from[51] and ^{177}Lu from[52]). Spatial transcriptomic expression maps were scaled with a 1:1 micron to pixel conversion and smoothed for continuous expression. DPKs were then convolved with the expression maps to hypothesize radiation density for genes of interest. mRNA expression was assumed to have a 1:1 correlation with cell-surface protein expression. Furthermore, it was assumed that a targeted radiotherapy binds specifically only to the target and remains on the target until it has completely decayed.

Transgenic mouse model[39]

To deconstruct the requirements for pancreatic cancer development from adult pancreatic cells, the Attardi laboratory has developed a $Kras^{LSL-G12D/+}$;$Rosa26^{LSL-tdTomato/LSL-tdTomato}$;$Ptf1a^{CreER}$ mouse model[39] by activating oncogenic $Kras^{G12D}$ and deleting $Trp53$ in mouse pancreatic cells with a tamoxifen-inducible knock-in $Ptf1a^{CreER}$ allele in mice on a C57BL/6 background with both genders. Tamoxifen was prescribed at 8–10 weeks of age. All mice are housed at a temperature range of 20–22 °C, humidity of 30–70%, with a diurnal light/dark cycle that switches at 7 am and 7 pm. Since the tumors are orthotopically induced in the body cavity with potential for metastasis, and tumor volume cannot be readily measured, body weight, signs of muscle atrophy and emaciation (body condition score), and general behavior was monitored 3 times per week. A weight loss of 20% or 15% for 72 h with a body condition score of < 2 was an endpoint for euthanasia and was within the guidelines of APLAC.

Radiolabeling

All radiolabeling experiments were conducted under the Controlled Radiation Authorization (CRA) approved by Stanford University. For the radiolabeling of DOTA-PEG$_2$-C4BP with ^{64}Cu ($t_{1/2}$ = 12.7 h), ^{64}CuCl$_2$ (74 MBq, 2 mCi; 0.1 M HCl) from Washington University was mixed with freshly prepared labeling buffer (200 μL, 0.1 M ammonium citrate/0.1 M ascorbic acid, pH 6.0). The peptide (2 nmol) was added to reach molar activity (74 MBq/nmol, 2 mCi/nmol). The reaction cocktail was then mixed at 600 rpm, 60 °C for 15 minutes, and the reaction progress checked by radio-TLC. The solid phase extraction cartridge (C18 SepPak plus light column) was pre-activated with 5 mL 99.9% ethanol followed by 10 mL water. The radiolabeled peptides were eluted from the cartridge with ~0.5–1 mL solution prepared with 1:1 volume ratio of 99.9 % EtOH:water. The eluted solution was diluted with 0.9% sterile NaCl with 10 mg/mL ascorbic acid (pH 7) until a final ethanol concentration reached less than 10%. Radiolabeling yield and radiochemical purity were analyzed with a TLC scanner (Bioscan) and HPLC (C18 column 4.6 × 250 mm, Phenomenex) connected to radiodetector, respectively. Non-decay corrected isolated yield, radio-TLC yield, and radiochemical purity in preliminary studies were (> 68%, >99%, >95%), respectively.

PET/CT, MR imaging and biodistribution

For PET/CT imaging, mice were anesthetized using 3.0% isoflurane in oxygen, maintained at 1.5–2.0% isoflurane, and subjected to ^{64}Cu-C4BP injections (126 ± 22 mCi (4.6 ± 0.8 MBq)/mouse). Images of $KPTC$:$Kras^{LSL-G12D/+}$;$Trp53^{fl/fl}$;$Rosa26^{LSL-tdTomato/LSL-tdTomato}$;$Ptf1a^{CreER}$ mouse model ($n = 6$) and age-matched wild type C57BL/6 mice ($n = 6$) were acquired at 0, 4, and 21 h post-injection. PET/CT (Inveon, Siemens) scanning for the 0 h time point started on the PET scanner bed with a simultaneous tail-vein injection of ^{64}Cu-C4BP for 30 minutes to obtain dynamic temporal images, then subsequently, CT imaging was acquired for 10 minutes for the anatomical reference. The following time-point scans were performed at 4 and 21 h. All 12 mice were scanned at 49 and 84 days after tamoxifen treatment to induce tumors. At 84 days, 6 mice ($n = 3$: KPTC, $n = 3$ wild-type control mice) were euthanized after PET/CT scans, and ex vivo PET imaging of organs such as liver, spleen, pancreas, colon and small intestines was performed. After collecting all organs of interest (blood, heart, lungs, spleen, stomach, feces, kidneys, muscle, bone, skin, and brain), radioactivity in each organ was measured using a gamma counter. The biodistribution of ^{64}Cu-C4BP is presented as percent injected activity per g (%IA/g) in organs. At 120 days, the remaining mice were imaged with PET/CT, and based on morbidity, were euthanized. One mouse showing significant weight loss was scanned under PET/CT and T2-weighted MRI, and a bright field image of the abdominal area was taken. T2-weighted MR images were acquired with an 11.7 T Agilent MR scanner with Bruker interface. Mice were oriented similar to PET/CT and scanned with a TR of 2500 msec and a TE of 3 msec with standard fat suppression T2-weighted fast spin-echo sequence with a slice thickness of 0.8 mm to capture the pancreas. Organs showing peritoneal metastasis were further analyzed with IHC and H&E.

Quantitative region of interest (ROI) analysis

PET image analysis was performed with Inveon Research Workplace (IRW) software after the co-registration of PET and CT images. Images were quantified by manually drawing regions-of-interest (ROI) in the hot spots adjacent to abdominal organs such as stomach, liver and kidney. Radioactivity in organs was normalized to the percent injected activity per cubic centimeter volume (%IA/cc).

Software

Rstudio with R version 4.2.2 was used for computation environment and language. Seurat v4 was used for spatial transcriptomic analysis and clusterProfiler v4 was used for enrichment analysis. Monocle3 was used for pseudotime analysis. Ggplot was used for plotting analysis results in R. Custom scripts were created for data wrangling between packages, MA plots, surfaceome score calculations, and mapping of pseudotime onto spatial dimension. Enable Medicine's online proprietary software and R package, Spatialmap, were used for multi-plexed IHC analysis.

Statistical analyses

Statistical analyses were completed using Graphpad Prism 9 (RRID:SCR_000306), RStudio 2023.09.1, and R version 4.2.2. Significance was assessed using an unpaired t-test and one-way ANOVA as described in the figure captions. Pearson's correlations were calculated with the correlation function in R (corr).

Reporting summary

Further information on research design is available in the Nature Portfolio Reporting Summary linked to this article.

Data availability

All data are available in Synapse.org database, and source data for the main figures is attached. A subset of IPMN spatial transcriptomic datasets (LG_1, LG_2, LG_3, LG_4, LG_5, LG_6, LG_7, HG_1, HG_2, HG_3 PDAC_1, PDAC_2, PDAC_3) were downloaded from NCBI GEO with an accession number: GSE233254 based on reference [23] [https://www.ncbi.nlm.nih.gov/geo/query/acc.cgi?acc=GSE233254]. A subset of PDAC spatial transcriptomic datasets (HT264P1, HT270P1, HT284P1, HT288P1, HT224P1, HT231P1, HT231P1-2, HT232P1, HT232P1-2, HT259P1, HT306P1, HT306P1-2, HT306P1-3, HT306P1-4, HT242P1) were downloaded from the HTAN Data Coordinating Center Data Portal at the NCI (https://humantumoratlas.org/explore) based on the reference[24]. These data are found in the atlas HTAN WUSTL as 10x Visium pancreatic cancer files. The files can be accessed directly using the shortened URL. Level 3 transcriptomic datasets from Stanford (STPDAC11, STPDAC12, STPDAC13, STPDAC14, STIPMN11, STIPMN12, STIPMN21, STIPMN22, STIPMN31, STIPMN32, STIPMN33, STIPMN34) in this study have been deposited in the Synapse.org database (created by Sage Bionetworks in partnership with scientific organizations) under accession code syn61831984. Level 3 datasets are a genomic terminology used by HTAN and others and refer to spatial transcriptomic datasets where derived biomolecular data are mapped to image positions and include barcodes, features, matrices, and corresponding histology image file. Access can be obtained by registering as a user at Synapse.org. The processed data are available as corresponding Source Data file. The processed transcriptomic data and CODEX data generated in this study are provided in the Supplementary Information/Source Data file. Source data are provided with this paper.

Code availability

Code for optimizing clustering parameters have been deposited onto Zenodo.org and can be accessed at [https://doi.org/10.5281/zenodo.13882933][53].

References

1. Bell, A. T. F. et al. PanIN and CAF transitions in pancreatic carcinogenesis revealed with spatial data integration. *Cell Systems* **15.8**, 753–769 (2024).
2. Carpenter, E. S. et al. Analysis of Donor Pancreata Defines the Transcriptomic Signature and Microenvironment of Early Neoplastic Lesions. *Cancer Discov.* **13**, 1324–1345 (2023).
3. Konstantinidis, I. T. et al. Incidentally discovered pancreatic intraepithelial neoplasia: what is its clinical significance? *Ann. Surg. Oncol.* **20**, 3643–3647 (2013).
4. Brosens, L. A., Hackeng, W. M., Offerhaus, G. J., Hruban, R. H. & Wood, L. D. Pancreatic adenocarcinoma pathology: changing "landscape". *J. Gastrointest. Oncol.* **6**, 358 (2015).
5. Siegel, R. L., Giaquinto, A. N. & Jemal, A. Cancer statistics, 2024. *CA: a cancer J. clinicians* **74**, 12–49 (2024).
6. Lennon, A. M. et al. Feasibility of blood testing combined with PET-CT to screen for cancer and guide intervention. *Science* **369**, eabb9601 (2020).
7. Pons-Belda, O. D., Fernandez-Uriarte, A. & Diamandis, E. P. Can circulating tumor DNA support a successful screening test for early cancer detection? the grail paradigm. *Diagnostics* **11**, 2171 (2021).
8. Cohen, J. D. et al. Detection and localization of surgically resectable cancers with a multi-analyte blood test. *Science* **359**, 926–930 (2018).
9. Röhrich, M. et al. Impact of 68Ga-FAPI PET/CT Imaging on the therapeutic management of primary and recurrent pancreatic ductal adenocarcinomas. *J. Nucl. Med.* **62**, 779–786 (2021).
10. Yang, T., Ma, L., Hou, H., Gao, F. & Tao, W. FAPI PET/CT in the diagnosis of abdominal and pelvic tumors. *Front. Oncol.* **11**, 797960 (2022).
11. Hu, Z. et al. The Cancer Surfaceome Atlas integrates genomic, functional and drug response data to identify actionable targets. *Nat. Cancer* **2**, 1406–1422 (2021).
12. Fujiwara-Tani, R. et al. Claudin-4: a new molecular target for epithelial cancer therapy. *Int. J. Mol. Sci.* **24**, 5494 (2023).
13. Shashikanth, N. et al. Tight junction channel regulation by inter-claudin interference. *Nat. Commun.* **13**, 3780 (2022).
14. Sasaki, T. et al. Targeting claudin-4 enhances chemosensitivity of pancreatic ductal carcinomas. *Cancer Med.* **8**, 6700–6708 (2019).
15. Lee, J. H. et al. Immunohistochemical analysis of claudin expression in pancreatic cystic tumors. *Oncol. Rep.* **25**, 971–978 (2011).
16. Joshi, S. et al. Genetically engineered mucin mouse models for inflammation and cancer. *Cancer Metastasis Rev.* **34**, 593–609 (2015).
17. Landers, K. A. et al. Identification of claudin-4 as a marker highly overexpressed in both primary and metastatic prostate cancer. *Br. J. Cancer* **99**, 491–501 (2008).
18. Kominsky, S. L. et al. Clostridium perfringens enterotoxin elicits rapid and specific cytolysis of breast carcinoma cells mediated through tight junction proteins claudin 3 and 4. *Am. J. Pathol.* **164**, 1627–1633 (2004).
19. Martín de la Fuente, L. et al. Claudin-4 expression is associated with survival in ovarian cancer but not with chemotherapy response. *Int J. Gynecol. Pathol.* **37**, 101–109 (2018).
20. Nichols, L. S., Ashfaq, R. & Iacobuzio-Donahue, C. A. Claudin 4 protein expression in primary and metastatic pancreatic cancer: support for use as a therapeutic target. *Am. J. Clin. Pathol.* **121**, 226–230 (2004).
21. Neesse, A. et al. Claudin-4-targeted optical imaging detects pancreatic cancer and its precursor lesions. *Gut.* **62**, 1034–1043 (2013).
22. Zhang, D., Huang, G., Liu, J. & Wei, W. Claudin18.2-targeted cancer theranostics. *Am. J. Nucl. Med Mol. Imaging* **13**, 64–69 (2023).
23. Sans, M. et al. Spatial transcriptomics of intraductal papillary mucinous neoplasms of the pancreas identifies NKX6-2 as a driver of gastric differentiation and indolent biological potential. *Cancer Discov.* **13**, 1844–1861 (2023).
24. Cui Zhou, D. et al. Spatially restricted drivers and transitional cell populations cooperate with the microenvironment in untreated and chemo-resistant pancreatic cancer. *Nat. Genet.* **54**, 1390–1405 (2022).
25. Peng, J. et al. Single-cell RNA-seq highlights intra-tumoral heterogeneity and malignant progression in pancreatic ductal adenocarcinoma. *Cell Res.* **29**, 725–738 (2019).
26. Jones R. C. et al. The Tabula Sapiens Consortium*. (2002). The Tabula Sapiens: a multiple-organ, single-cell transcriptomic atlas of humans. *Science* **376**, 6594 (2022).
27. Stuart, T. et al. Comprehensive integration of single-cell data. *Cell* **177**, 1888–1902.e1821 (2019).
28. Liberzon, A. et al. The molecular signatures database hallmark gene set collection. *Cell Syst.* **1**, 417–425 (2015).
29. Crnogorac-Jurcevic, T. et al. Molecular alterations in pancreatic carcinoma: expression profiling shows that dysregulated expression of S100 genes is highly prevalent. *J. Pathol.* **201**, 63–74 (2003).
30. Wu, Y. et al. S100 proteins in pancreatic cancer: current knowledge and future perspectives. *Front Oncol.* **11**, 711180 (2021).
31. Hu, F. et al. IL-17 in pancreatic disease: pathogenesis and pharmacotherapy. *Am. J. Cancer Res.* **10**, 3551–3564 (2020).
32. Hoffmann, W. TFF2, a MUC6-binding lectin stabilizing the gastric mucus barrier and more (Review). *Int J. Oncol.* **47**, 806–816 (2015).
33. Elyada, E. et al. Cross-species single-cell analysis of pancreatic ductal adenocarcinoma reveals antigen-presenting cancer-associated fibroblasts. *Cancer Discov.* **9**, 1102–1123 (2019).
34. Öhlund, D. et al. Distinct populations of inflammatory fibroblasts and myofibroblasts in pancreatic cancer. *J. Exp. Med.* **214**, 579–596 (2017).
35. Han, C., Liu, T. & Yin, R. Biomarkers for cancer-associated fibroblasts. *Biomark. Res.* **8**, 64 (2020).
36. Zhang, T., Ren, Y., Yang, P., Wang, J. & Zhou, H. Cancer-associated fibroblasts in pancreatic ductal adenocarcinoma. *Cell Death Dis.* **13**, 897 (2022).
37. Vecchio, A. J., Rathnayake, S. S. & Stroud, R. M. Structural basis for Clostridium perfringens enterotoxin targeting of claudins at tight junctions in mammalian gut. *Proc. Natl. Acad. Sci. USA.* **118**, e2024651118 (2021).
38. Ling, J., Liao, H., Clark, R., Wong, M. S. & Lo, D. D. Structural constraints for the binding of short peptides to claudin-4 revealed by surface plasmon resonance. *J. Biol. Chem.* **283**, 30585–30595 (2008).
39. Flowers, B. M. et al. Cell of origin influences pancreatic cancer subtype. *Cancer Discov.* **11**, 660–677 (2021).
40. Tsutsumi, K. et al. Expression of claudin-4 (CLDN4) mRNA in intraductal papillary mucinous neoplasms of the pancreas. *Mod. Pathol.* **24**, 533–541 (2011).
41. Torres, J. B. et al. Imaging of claudin-4 in pancreatic ductal adenocarcinoma using a radiolabelled anti-claudin-4 monoclonal antibody. *Mol. Imaging Biol.* **20**, 292–299 (2018).
42. Torres, J. B. et al. Radiolabeled cCPE peptides for SPECT imaging of claudin-4 overexpression in pancreatic cancer. *J. Nucl. Med.* **61**, 1756–1763 (2020).
43. Ganguly, T. et al. Preclinical Evaluation of (68)Ga- and (177)Lu-Labeled Integrin α(v)β(6)-Targeting Radiotheranostic Peptides. *J. Nucl. Med.* **64**, 639–644 (2023).
44. Quigley, N. G. et al. PET/CT imaging of head-and-neck and pancreatic cancer in humans by targeting the "cancer integrin" αvβ6

with Ga-68-Trivehexin. *Eur. J. Nucl. Med Mol. Imaging* **49**, 1136–1147 (2022).

45. Dash, A., Chakraborty, S., Pillai, M. R. & Knapp, F. F. Jr. Peptide receptor radionuclide therapy: an overview. *Cancer Biother Radiopharm.* **30**, 47–71 (2015).

46. Strosberg, J. et al. Phase 3 trial of (177)Lu-dotatate for midgut neuroendocrine tumors. *N. Engl. J. Med.* **376**, 125–135 (2017).

47. Morris, M. J. et al. Phase III study of lutetium-177-PSMA-617 in patients with metastatic castration-resistant prostate cancer (VISION). *J. Clin. Oncol.* **39**, LBA4–LBA4 (2021).

48. Wu, T. et al. clusterProfiler 4.0: A universal enrichment tool for interpreting omics data. *Innovation* **2**, 100141 (2021).

49. Patel, A. P. et al. Single-cell RNA-seq highlights intratumoral heterogeneity in primary glioblastoma. *Science* **344**, 1396–1401 (2014).

50. Schneider, M. K. et al. Combined near infrared photoacoustic imaging and ultrasound detects vulnerable atherosclerotic plaque. *Biomaterials* **302**, 122314 (2023).

51. Peter, R. et al. Small-scale (sub-organ and cellular level) alpha-particle dosimetry methods using an iQID digital autoradiography imaging system. *Sci. Rep.* **12**, 17934 (2022).

52. Graves, S. A., Flynn, R. T. & Hyer, D. E. Dose point kernels for 2,174 radionuclides. *Med. Phys.* **46**, 5284–5293 (2019).

53. Cluster tuner for Spatial transcriptomic analysis drives PET imaging of tight junction protein expression in pancreatic cancer theranostics (Zenodo, https://doi.org/10.5281/zenodo.13882933, 2024).

Acknowledgements

Author contributions

J.W., A.J.K., J.W.S. and K.W.F. designed and implemented the study and wrote the paper. G.C. and M.S. provided samples and pathological interpretation. W.P., R.B. and A.I. provided clinical guidance on the study design and image interpretation. M.P., S.T., B.W. G.E., N.Z., Y.G. and M.R. performed experiments. S.F. and L.A. developed and characterized the mouse models. X.Z. and G.P. provided guidance on therapeutic simulations.

Competing interests

The authors declare no competing interests.

Additional information

Supplementary information The online version contains supplementary material available at https://doi.org/10.1038/s41467-024-54761-6.

Correspondence and requests for materials should be addressed to Katherine W. Ferrara.

Peer review information *Nature Communications* thanks Xianlu Peng, Youqiong Ye and the other, anonymous, reviewer(s) for their contribution to the peer review of this work. A peer review file is available.

Reprints and permissions information is available at http://www.nature.com/reprints

Publisher's note Springer Nature remains neutral with regard to jurisdictional claims in published maps and institutional affiliations.